Nanoscale

PAPER

View Article Online
View Journal

Cite this: DOI: 10.1039/d6nr00994h

Tunable opto-magnetic metamaterials *via* coupled TiN–NiO vertically aligned nanocomposite thin films

Natalia Garcia Godinez, [a] Jiawei Song,[a] Yizhi Zhang, [a] Amirr Dion Neal,[a] Claire A. Mihalko, [a] Lizabeth Quigley, [a] Juanjuan Lu, [a] Ping Lu [b,c] and Haiyan Wang *[a,d]

Received 11th March 2026,
Accepted 22nd May 2026

DOI: 10.1039/d6nr00994h

rsc.li/nanoscale

The integration of plasmonic and magnetic properties in self-assembled hybrid metamaterials offers new opportunities for tunable light–matter interactions in nanoscale thin films. We report a systematic study on laser pulse frequency as a parameter for tuning the microstructure-dependent optical anisotropy and magnetic response in vertically aligned nanocomposites (VANs) composed of plasmonic titanium nitride (TiN) and dielectric nickel oxide (NiO). Using pulsed laser deposition (PLD), TiN–NiO VAN thin films were grown on MgO(001) substrates at various laser frequencies (*i.e.*, 2, 5, and 10 Hz) while keeping all other growth parameters consistent. Structural and morphological analysis reveal that NiO pillar density increases with pulse frequency, enabling controlled modulation of the VAN structure. Ellipsometry data shows that all samples exhibit Type-II hyperbolic dispersion with increased optical anisotropy for samples deposited under higher frequencies. Magnetic hysteresis measurements demonstrate ferromagnetic behavior at both 10 K and 300 K, with enhanced coercivity and out-of-plane anisotropy that correlates with pillar morphology. This tunability allows for enhanced control over the optical and magnetic responses of hybrid metamaterials, enabling the insurgence of novel technologies for data storage, communication, and optoelectronic devices.

1 Introduction

Metamaterials are artificially engineered nanostructures with subwavelength features that enables new areas of light–matter interaction by combining materials with functions different from their bulk composition.[1] These materials exhibit optical phenomena arising from the excitation of surface plasmon polaritons (SPPs) and localized surface plasmons (LSPs), which harness the collective oscillations of charge carriers under incident illumination.[2–4] The relationship between optical and magnetic phenomena in metamaterials has inspired interest for engineering light–matter interaction, particularly for applications in reconfigurable photonics and spintronic devices.[5–8] The interplay of opto-magnetic materials enables functionalities such as ultrafast all-optical magnetic switching for high-speed memory, hybrid opto-magnetic effects, and light controlled spin injection in spintronic circuits.[9]

Beyond the demonstrations of single phase metamaterials, hybrid metamaterials (HM) made of two or more materials in an artificial morphological arrangement have drawn great interest due to their unique optical responses and electromagnetic functionalities.[10] Examples include Ag nanowires embedded in alumina (Al_2O_3) matrix prepared through electrochemical anodization,[11] demonstrating negative refraction at visible wavelengths, Au split-ring resonators (SRRs) on glass processed by focused ion beam[12] and classic Ag–MgF_2–Ag fishnets processed by electron-beam lithography.[13]

Recently, vertically aligned nanocomposites (VANs) have emerged as a compelling class of hybrid metamaterials due to their unique vertically aligned phase morphology, intrinsic anisotropy, integrated functionalities, strain coupling, and one-step self-assembly during deposition.[14–18] VANs form through self-assembly driven by different nucleation behaviors of the two film phases: one phase adopts a layered growth mode while the second phase prefers island nucleation, resulting in vertically aligned nanopillars embedded within a continuous matrix.[17,19] VAN thin films have been documented in a variety of different systems, including oxide–oxide VANs, nitride–metal VANs, oxide–metal VANs, and other complex multi-phase systems. In many oxide-based VANs, such as $BaTiO_3$: $CoFe_2O_4$

[a]*School of Materials Engineering, Purdue University, West Lafayette, Indiana 47907, USA*
[b]*Sandia National Laboratories, Albuquerque, New Mexico 87185, USA*
[c]*Center for Integrated Nanotechnologies, Sandia National Laboratories, Albuquerque, New Mexico 87185, USA*
[d]*School of Electrical and Computer Engineering, Purdue University, West Lafayette, Indiana 47907, USA. E-mail: hwang00@purdue.edu*

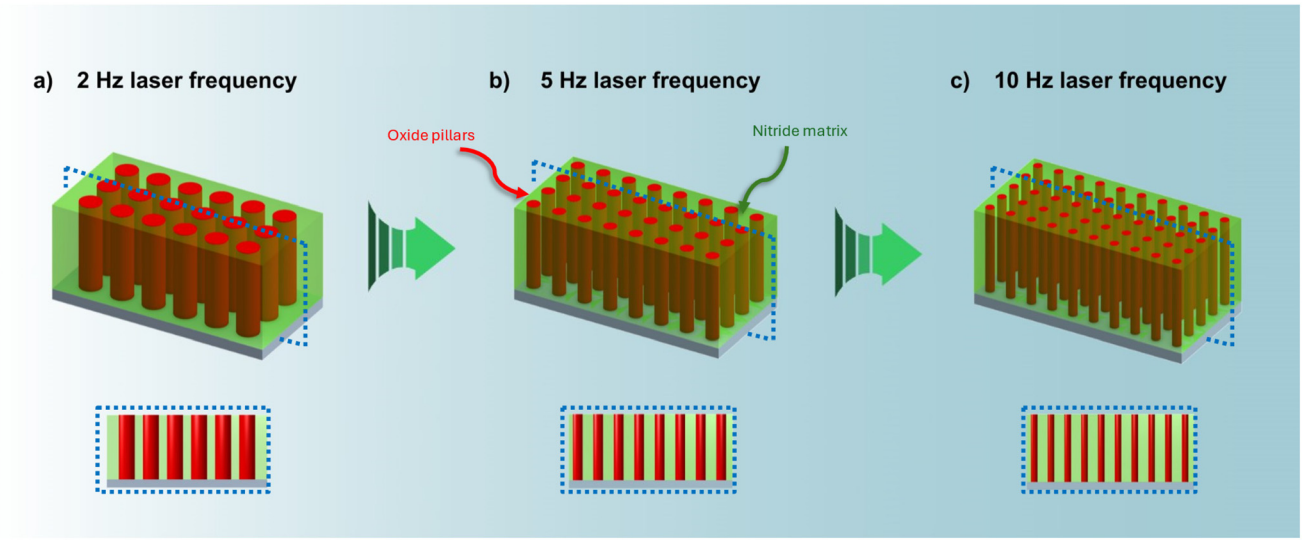

Fig. 1 Schematic illustration of vertically aligned TiN–NiO nanocomposite structures deposited at varying laser pulse frequencies (a) 2 Hz, (b) 5 Hz, and (c) 10 Hz. Insets display cross-sectional views highlighting evolution as frequency increases.

(BTO–CFO) and $BiFeO_3:CoFe_2O_4$ (BFO–CFO), the pillar density, aspect ratio, and interfacial coupling have been finely tuned by modifying growth parameters or target composition.[20–23] These studies establish a foundation for extending VAN design into underexplored nitride–oxide systems, where plasmonic, magnetic, and anisotropic optical multifunctionalities could be integrated within a complete ceramic-based VAN system.[17,24,25]

Given their structural anisotropy, VANs are promising candidates for hyperbolic metamaterials (HMMs), which exhibit anisotropic dielectric responses.[1,26] By engineering dielectric anisotropy, VANs exhibit tunable HMM behavior across a broad spectral range.[2,24,27] Traditional metal-dielectric HMM VANs, such as Au-BTO or Au-$La_{0.67}Sr_{0.33}MnO_3$ (LSMO), are well established for their strong optical tunability.[25,28] These systems have laid important groundwork for understanding light–matter interactions in anisotropic VANs. Building on this, recent efforts have shifted toward nitride-based heterostructures that retain metal-like optical responses while offering enhanced thermal stability, and additional magneto-optical functionality under harsh conditions.[18,29,30]

In this work, we demonstrate the growth of epitaxial TiN–NiO as a nitride–oxide-based VAN thin film with tunable HMM behaviors. The films were deposited on MgO substrates using pulsed laser deposition (PLD) and compared with a TiN reference film. TiN is selected as the matrix phase considering its plasmonic properties and superior chemical and thermal stability compared to noble metals such as Ag and Au.[29,31] TiN-based plasmonic structures exhibit lower optical losses at elevated temperature and enhanced resilience in harsh environments, positioning TiN as a robust alternative for practical photonic and optoelectronic devices.[32] Nickel oxide (NiO), although antiferromagnetic at bulk, has displayed weak nanoscale ferromagnetism due to surface spin effects, lattice distortions, and interfacial coupling.[33,34] Kodama *et al.* demonstrated that NiO in the 6–80 nm size range displays anomalous magnetic behavior, including large net moments and coercivities and even hysteresis loop shifts of up to 10 kOe, which are attributed to finite size induced spin configurations.[35] Previous studies have shown that when embedded as nanopillars in a TiN matrix, the resulting heterostructure exhibits broadband hyperbolic dispersion and emergent magneto-optical coupling.[36,37]

However, unlike prior frequency dependent studies,[28,38,39] the tunability of a plasmonic-magnetic ceramic (oxide) – ceramic (nitride) VAN remains unexplored. In this study, we investigate the effect of laser pulse frequency during PLD on the tunability of dielectric anisotropy and magnetic response in TiN–NiO VAN thin films. By controlling growth kinetics through laser pulse frequency, it is expected that the pillar density and dimensions will be systematically modified as illustrated in the schematic in Fig. 1. The microstructure was characterized by X-ray diffraction (XRD) and transmission electron microscopy (TEM) analysis. Spectroscopic ellipsometry and magnetic hysteresis measurements were conducted to evaluate the corresponding changes in hyperbolic optical response and magnetic behavior. This study provides insight into oxide–nitride VANs and opens new routes toward deposition-driven tunability in complex all-ceramic hybrid metamaterial systems.

2 Results and discussion

Three TiN–NiO nanocomposite thin films were deposited on single-crystal MgO(001) substrates using PLD, considering the close lattice parameter matching of MgO (a = 4.21 Å), TiN (a = 4.24 Å), and NiO (a = 4.17 Å) to facilitate epitaxial growth and

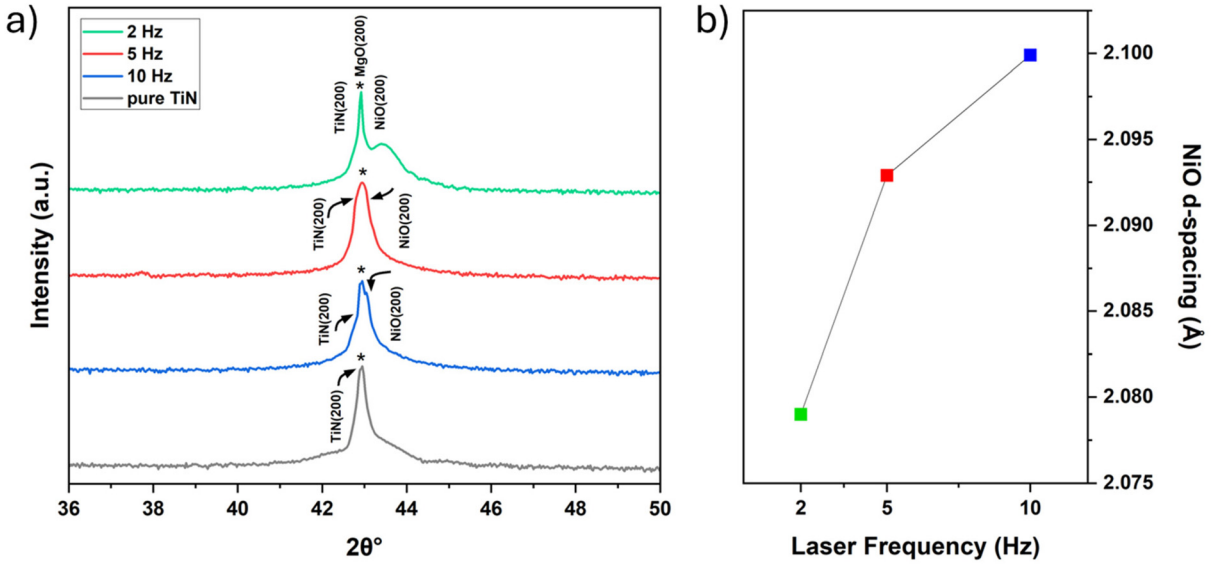

Fig. 2 (a) θ–2θ XRD patterns of TiN–NiO thin films grown on MgO(200) substrate under 650 °C with variable laser frequency during deposition and (b) *d*-spacing of NiO XRD peaks as laser deposition frequency increases.

coherent interfaces. The phase composition of the thin films was characterized using θ–2θ X-ray diffraction (XRD) scans. Fig. 2a shows the θ–2θ scans of the films as deposition frequency increases, along with a pure TiN thin film as comparison. All TiN–NiO samples display similar TiN(200) and NiO (200) peaks appearing as shoulder peaks adjacent to the dominant MgO(200) substrate peak. Selected area electron diffraction (SAED) pattern in Fig. S2 confirms the epitaxial growth of the TiN matrix and NiO nanopillars on the MgO(001) substrate and their epitaxial relationship as cube-on-cube growth of all three phases.

It is noted that the NiO(200) peak systematically shifts to lower 2θ values as pulse frequency increases. This indicates an increase in the out-of-plane *d*-spacing in the vertical direction, as shown in Fig. 2b. This trend suggests that higher laser frequencies lead to greater tensile strain in the NiO pillars, which are likely due to a higher deposition rate at increased laser frequencies. Under these conditions, adatom mobility is reduced, limiting strain relaxation time and promoting vertical tensile strain of the NiO pillars. In contrast, TiN(200) peak remains nearly unchanged, suggesting the TiN matrix presents less strain due to the NiO pillars. Interestingly, a weak NiO(111) peak was observed exclusively in the 5 Hz sample, suggesting the presence of crystals with the (111) orientation. The absence of this peak in the 2 Hz and 10 Hz samples may be due to a preferred NiO(200) growth. These observations support a strain driven process of nanostructure formation, where interfacial lattice mismatch and surface energy minimization lead the self-assembly and morphological evolution of the VAN structure.[24,40]

To further understand the orientation and morphology of the NiO and TiN phases and their epitaxial relationship, the VAN structures were investigated using scanning electron transmission microscopy (STEM) and energy-dispersive X-ray spectroscopy (EDS) mapping. Phase separation was evaluated with cross-sectional EDS and STEM under the high-angle annular dark-field (HAADF) mode for all three samples as shown in Fig. 3. The results demonstrate that vertical alignment and epitaxial growth with the MgO(001) substrate is maintained across all frequencies. We observe a morphological trend, meaning that the NiO pillars become thinner and more densely packed as laser pulse frequency increases. Table S1 summarizes the film thickness and estimated pillar areal density as a function of laser frequency, as quantified from the cross-section and plan-view STEM and EDS images in Fig. 3 and 4, respectively. The pillar areal density was approximated using combined cross-sectional and plan-view STEM analysis, assuming an effective TEM lamella thickness of ~20 nm. This trend in pillar density tuning is consistent with known kinetic effects in PLD where increasing laser frequency could shorten the pulse interval, which in return increases the growth rate and reduces the surface diffusion time available for adatom diffusion and nucleation. As demonstrated in other VAN systems (*e.g.*, ZnO–Au and LSMO–ZnO), this promotes high nucleation density and inhibits lateral growth, yielding finer pillar spacing.[41,42] This is further supported by XRD data showing a shift of the NiO(200) peak to lower 2θ values, indicating increased out-of-plane *d*-spacing and tensile strain in the NiO phase due to vertical strain coupling. The resulting shift in growth dynamics favors higher nucleation density over lateral growth, which yields more finely spaced nanopillars.

To confirm the self-assembled pillar formation and phase separation between the two materials, plan-view images for the representative TiN–NiO sample deposited at 5 Hz are shown in Fig. 4. HAADF-STEM images (Fig. 4a–c) were acquired at multiple magnifications, revealing a dense and uniform distri-

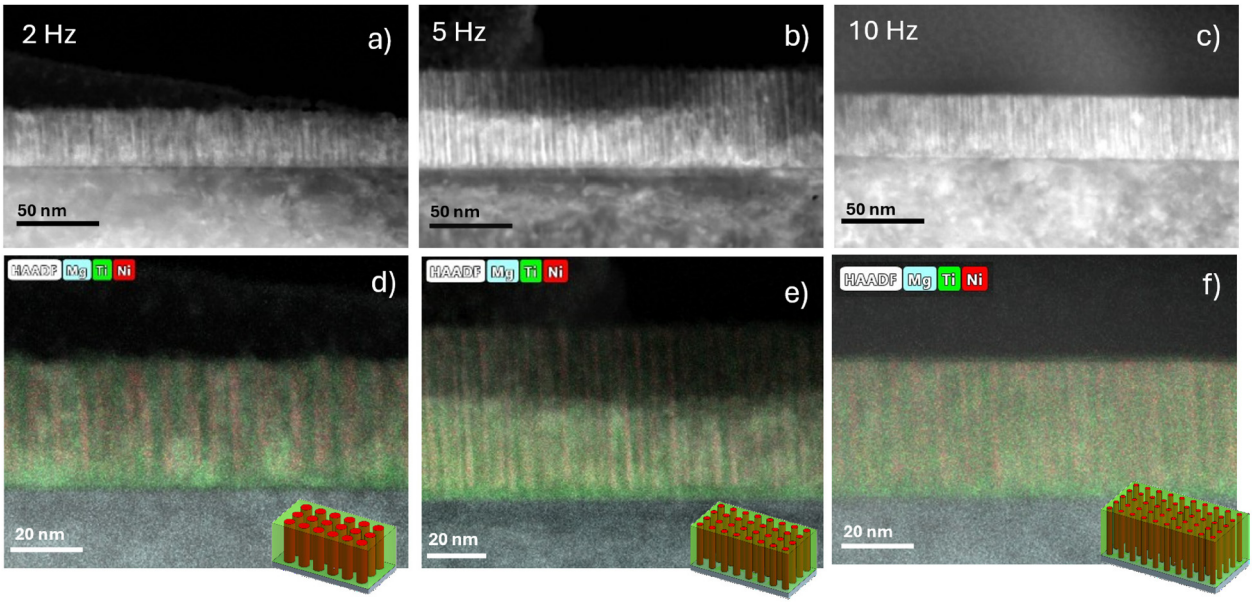

Fig. 3 Cross-sectional STEM images of corresponding vertically aligned nanostructures (VAN) grown at (a) 2 Hz, (b) 5 Hz, and (c) 10 Hz laser frequency, and (d–f) EDS elemental mapping of Mg, Ti, and Ni.

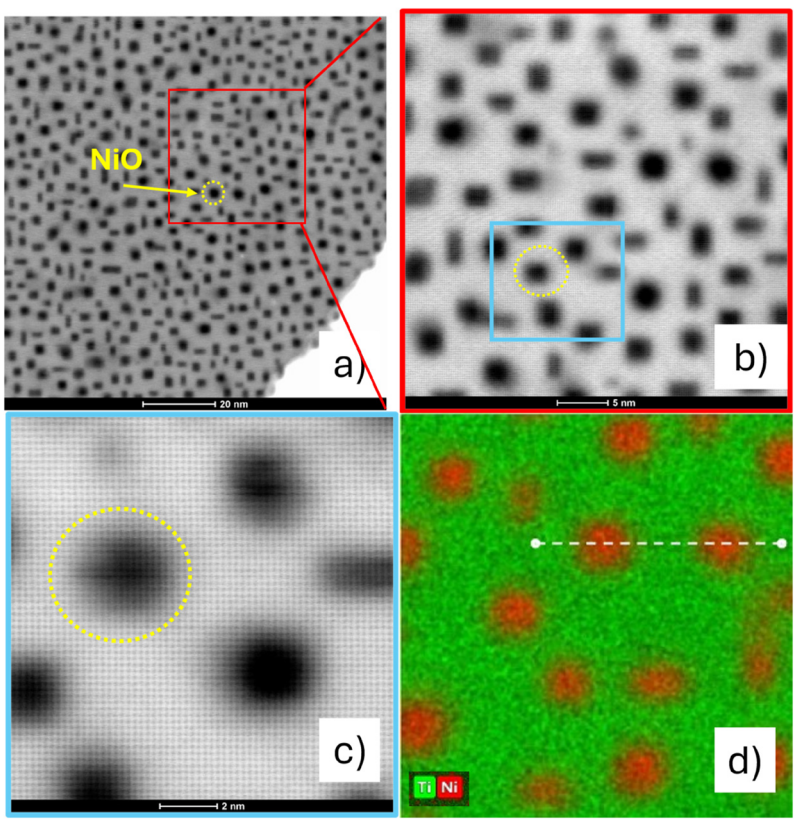

Fig. 4 Plan-view HRTEM images of TiN–NiO thin films deposited at laser frequency of 5 Hz on MgO(200) substrate (a) low magnification (b) medium magnification (c) high magnification resolution (d) EDS mapping of TiN matrix (green) and NiO pillars (red).

bution of NiO nanopillars embedded within the TiN matrix. The NiO pillars exhibit circular to slightly faceted morphologies with an average diameter of 2.83 ± 0.6 nm. A histogram of pillar diameter distribution was quantified and can be found in Fig. S4. This size places well within the regime where circular morphology dominates due to surface area minimization, consistent with reports that pillars with diameters below the critical dimension ($d = 4r$) adopt round shapes due to the balance between surface and elastic energies.[20,24] The high density of small pillars contributes to a relatively high interface area between TiN and NiO phases, which directly influence the vertical strain in the system. As reported in previous literature, vertical strain (ε) is inversely proportional to pillar size ($\varepsilon \propto 1/d$) under fixed volume fraction conditions.[20] The average volume fraction of NiO was estimated to be 23%, confirming the sample lies within a region where increasing the interfacial area can induce out-of-plane strain within matrix and pillar phases. The strong Z contrast between the phases enables a clear distinction between the matrix and the pillars. The TiN matrix appears bright due to the higher average atomic number, while the NiO pillars exhibit darker contrast. A yellow circle embedded in the figures highlights one representative NiO pillar. Elemental mapping in Fig. 4d and line profiles in Fig. S5 further confirm phase separation, where Ni-rich regions align with the pillar geometry, and Ti signals dominate in the surrounding matrix. Minimal overlap is observed between Ti and Ni signals, indicating sharp phase separation and minimal cation intermixing in the pillar-matrix interfaces. To confirm the composition of the NiO pillars, plan-view high resolution STEM analysis was conducted and one such image is shown in Fig. S6. This revealed well-ordered and continuous lattice-fringes extending across the pillar-matrix interface, suggesting nearly perfect coherent growth between the NiO pillars and TiN matrix. Lattice-fringe measurements within six different pillar regions reveal values $d_{\text{pillarNiO(200)}}$ = 0.2116 ± 0.0029 nm consistent with bulk rock-salt NiO (a = 4.17 Å and $d_{\text{bulk NiO(200)}}$ = 0.2085 nm) (JCPDS No. 47-1049) and exhibiting only minimal in-plane lattice distortion. The measured values are much larger than those expected for metallic Ni ($d_{\text{Ni(200)}}$ = 0.176 nm) and do not match known Ni–Ti lattice parameters, therefore supporting the formation of the NiO pillar phase rather than pure metallic Ni or alloyed phases.[43,44] Relative to bulk NiO, the measured lattice spacing correspond to strain of +1.49% along the (200) plane. The slight deviations from bulk NiO lattice parameters could be associated with local oxygen vacancies or strain effects from the surrounding TiN matrix. Based on the d-spacing analysis results of the high-resolution STEM images of the nanopillars and the matrix along with the optical response discussed below, it is more appropriate to identify the nanopillars as oxygen-deficient rock-salt NiO_x than that of FCC metallic Ni. These results demonstrate that PLD enables the self-assembly of highly ordered NiO pillars in TiN matrix with distinct phase separation. Variations in laser frequency effectively tune the pillar morphology and density *via* adatom mobility and growth kinetics. The observed morphological evolution can be directly linked to the changes in vertical strain in the NiO pillars, as confirmed by XRD peak shifts.

Since nanopillar morphology and interface density are expected to influence the dielectric response of the nanostructure by tuning plasmonic interactions within the TiN–NiO system, the anisotropic optical response of the thin films was measured on all three films *via* variable-angle spectroscopy ellipsometry using a J.A. Woollam RC2 system. Pure TiN is expected to behave as a metal, while NiO is expected to demonstrate dielectric behavior. TEM analysis revealed structural symmetry along the x and y directions, so the data was fitted with a biaxial model along with a general oscillator to capture in-plane and out of plane optical properties.

As mentioned previously, HMMs are materials whose dielectric permittivity components have opposite signs, which results in open isofrequency surfaces in momentum space, characteristics of high-k mode propagation. There are two principal types of hyperbolic dispersion commonly discussed: Type-I HMMs exhibit positive in-plane (IP $\varepsilon_{\parallel}$) and negative out-of-plane (OP $\varepsilon_{\perp}$) permittivity, while Type-II HMMs display the converse configuration.[1,45,46] Upon ellipsometry data analysis and fitting, all samples exhibit Type-II hyperbolic dispersions in the measured wavelength range The epsilon-near-zero (ENZ) points mark the wavelength where the real part of the permittivity crosses zero, which signifies a transition in optical responses. As shown in Fig. 5, the TiN–NiO VAN display clear differences in optical dispersion as a function of laser pulse frequency. The 2 Hz sample exhibits a broad Type-II hyperbolic region over much of the measured wavelength range, from 1050 nm to 2500 nm. While the 5 Hz sample displays a slight decrease in the Type-II hyperbolic region ranging from 1050 to 2250 nm, the 10 Hz sample displays the highest degree of optical anisotropy, with the Type-II region ranging from 500 to 2500 nm. In this system, the distinct ENZ points along the IP and OP directions are additional evidence of hyperbolic behavior, and the ability to tune with deposition frequency highlights the strong role of interface density as they relate to light–matter interactions. Although Type-II hyperbolic dispersion is more often reported in multilayer metamaterials,[27,47] its emergence in VAN structures may result from the vertically aligned dielectric NiO pillars (OP) and the metallic TiN as the matrix structure (IP) and sharp dielectric contrast between the two phases, mimicking the anisotropic effective media conditions needed for Type-II behavior.

The IP optical behavior was further investigated, and the real and imaginary components of the dielectric function were analyzed in Fig. S7 and extracted from ellipsometry fits using a biaxial general oscillator model. The real part (ε_1) represents how a material polarizes in response to an electric field. All films exhibit metallic behavior due to TiN ($\varepsilon_1 < 0$) across the measured spectral range, which is consistent with the metallic in plane behavior caused by the continuous TiN matrix, but the behavior varies with laser deposition frequency. The imaginary permittivity (ε_2) represents the degree of optical absorption and plasmonic damping. As observed, all nanocomposites show reduced absorption when compared to pure TiN, which

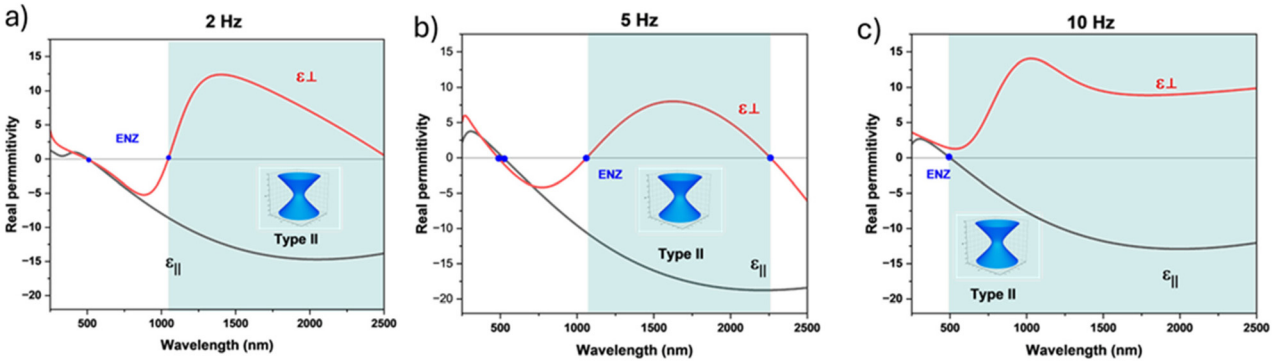

Fig. 5 In-plane ($\varepsilon_{\|}$) and out-of-plane ($\varepsilon_{\perp}$) permittivity for TiN–NiO VANs with a laser deposition frequency of (a) 2 Hz, (b) 5 Hz, and (c) 10 Hz. ENZ crossing points are marked in blue.

shows the highest ε_2 and likewise meaning that it has the highest optical loss. This indicates that the coupling TiN and NiO reduces energy dissipation and potentially improves plasmonic quality. Among all the deposited VAN films, the 5 Hz sample exhibits strongest absorption, while the 2 and 10 Hz sample remain comparable. These results are further evidence that laser pulse frequency acts as a processing parameter that tunes the VAN nanostructure, which in turn controls the effective dielectric anisotropy and optical loss.

To further study the magnetic behavior and tunability with varying laser frequency of TiN–NiO thin films, magnetizations (M) *vs.* magnetic field (H) measurements were conducted with applied external magnetic field in plane (IP) and out of plane (OP) to the films at both room temperature (300 K) and low temperature (10 K). As shown in Fig. 6(a–d), all TiN–NiO films exhibit weak ferromagnetic-like hysteresis loops (M–H) at 10 K and 300 K, indicating stable spin configurations across a wide thermal range, while the pure TiN film shows no obvious response as shown in Fig. S9. The top panels (a, b) represent the IP measurements at 10 K (a) and 300 K (b), while panels (c, d) present the OP measurements. Schematic illustrations of the direction of the measurement, indicating IP or OP, are

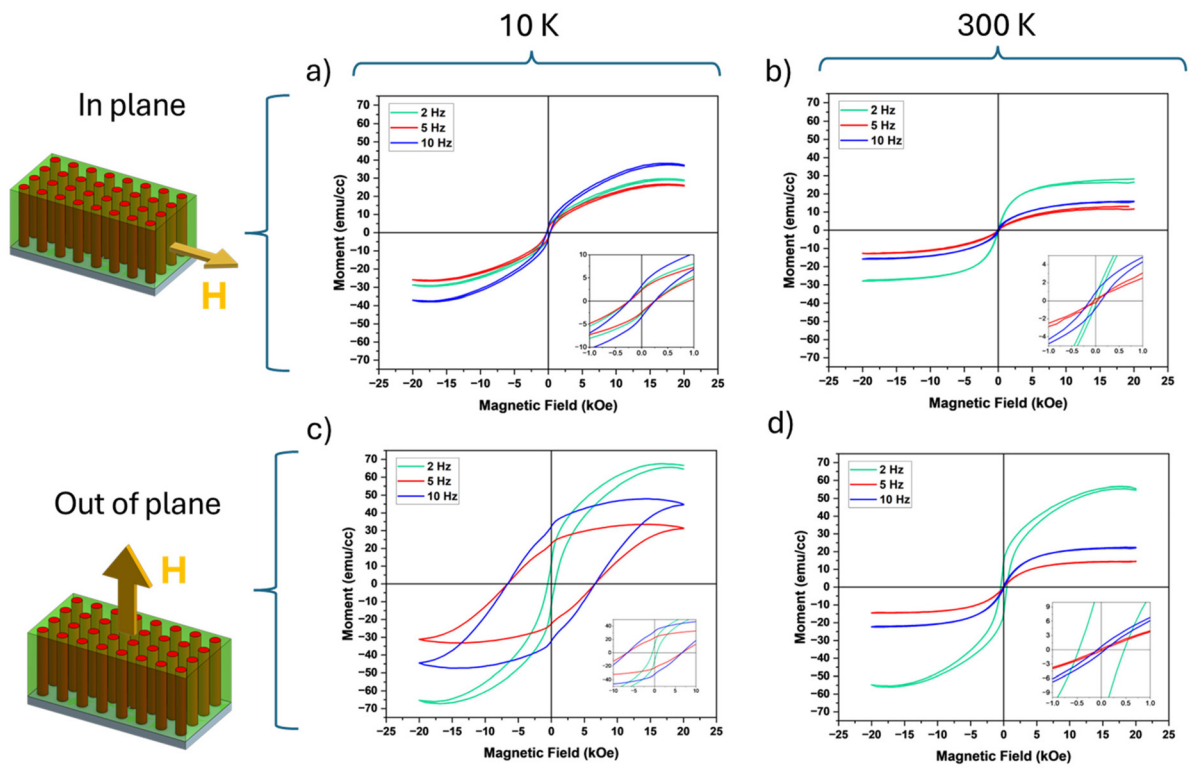

Fig. 6 Magnetic response of TiN–NiO thin films grown on MgO(200) substrate under 650 °C with different laser frequencies. (a) In-plane measured at 10 K, (b) in-plane measured at 300 K, (c) out-of-plane measured at 10 K. (d) Out-of-plane measured at 300 K (correction factors applied).

included and insets represent a selected enlarged area to better identify the coercivity.

In the IP direction, all samples maintain a comparable coercive field (H_c) in the range of −0.225 kOe and 0.225 kOe at low temperature with only the saturation moment (M_s) varying slightly. At 300 K, the films show an even weaker coercive field with slight variation in both H_c and M_s. However, in the OP direction, the samples exhibit a clearer magnetic hysteresis with moderate coercivity. The 5 and 10 Hz samples remain comparable, while the 2 Hz sample retains a higher and stable saturation moment with low coercivity at both low and high temperatures, indicating a robust but soft magnetic anisotropy that is absent in the 5 and 10 Hz films. Notably, the 2 Hz sample displays the highest saturation moment in the out of plane configuration although it has the weakest coercivity, which may result from larger NiO pillars facilitating more uncompensated spins due to the increased surface area and strain effects. The hysteresis loop shape of the 2 Hz sample remains nearly identical between low and high temperatures, which suggests thermally stable ordering. In contrast, the samples deposited at higher frequencies exhibit stronger OP coercivity and remanence compared to IP.

Temperature-dependent magnetization measurements were conducted on the 5 and 10 Hz samples, and they reveal a clear blocking transition which confirms that the films possess sufficient magnetic anisotropy to stabilize pin alignment against thermal fluctuations. The separation between field-cooled (FC) and zero-field-cooled (ZFC) curves highlights the influence of interfacial exchange in promoting anisotropic spin ordering. The results in Fig. S10 support the hysteresis data by confirming that the ferromagnetic response is governed by magnetic anisotropy.

By observing the evolution of the pillar morphology, we were able to gain insight into the preferred growth conditions for defined, high-quality phase separation of the two phases and the geometric variation of the pillars in a single film. The study demonstrates how the changes in interpillar distance and size act on tuning the dielectric function of the film and ultimately the hyperbolic range of the material, as well as the ferromagnetic-like behavior in the NiO pillars. This behavior is in good agreement with previous reports of enhanced coercivity and non-zero magnetic moment in nanoscale NiO, where finite-size and surface effects can generate ferromagnetic-like behavior.[35,48] As stated previously, bulk NiO is antiferromagnetic with fully compensated Ni^{2+} spins aligned in opposite sublattices. At the nanoscale, particularly below ~20 nm, uncompensated surface spins and broken sublattice symmetry give rise to a weak ferromagnetic component. As reported, particles below 10 nm exhibit increased coercivity and saturation magnetization due to enhanced surface spin disorder and sublattice reconstruction due to finite size.[49] The NiO pillars presented are confined to lateral dimensions below 10 nm and exhibit similar non-zero net moment, likely due to uncompensated spins at the pillar/matrix interfaces. The interface between NiO and metallic TiN may also act as an effective ferromagnetic/antiferromagnetic (FM/AFM) boundary, which gives rise to exchange bias phenomena observed in similar core–shell Ni/NiO systems.[33] The *M*–*H* hysteresis loops measured show that the anisotropic field, coercivity (H_c) and remanent magnetization (M_r) can be systemically tuned through growth kinetics.

Overall, this self-assembled nitride–oxide VAN system has proven its great potential in achieving tunable optical and magnetic properties, broadening the family of VANs and providing coupled properties. TiN has been previously integrated with other phases as various VAN structures, such as TiN–Au, TiN–Fe, TiN–Au–CoFe, where TiN forms the continuous plasmonic matrix hosting vertically aligned nanopillars.[18,31,50–52] However, the integration of plasmonic nitride with other oxide phases within a single VAN remains underexplored, offering new opportunities to investigate coupled optical and magnetic properties. An earlier study has demonstrated the formation of NiO nanorods in a TiN matrix forming TiN–NiO VAN thin films.[36] The work demonstrated hyperbolic dispersion and magneto-optical coupling in TiN–NiO systems through room-temperature polar and longitudinal MOKE measurements. However, the extent of the tunability demonstrated was limited. This could be due to the relatively thin (~18 nm) films grown and limited vertical interfaces. The thicker nitride–oxide VAN films investigated in this work fill that gap by showing the power of vertical interfaces in tuning of the overall film morphology as well as their optical and magnetic properties. The laser deposition frequency effectively tunes adatom flux, surface diffusion, epitaxy, and interface qualities. These parameters govern the vertical alignment, pillar density, strain state, and thus the physical properties of the VAN system. Future work could extend this strategy to other oxide–nitride systems to develop multifunctional, thermally stable photonic platforms, while expanding optical characterization beyond the current range could help better define the tuning limits of VAN-based photonic platforms. Additional studies could include further exploration of other lattice-matched or lattice mismatched oxides in a nitride matrix, expanding the films to integrate with other substrates such as $SrTiO_3$ and Si, or other buffers for free-standing thin films.[53–55]

3 Conclusion

To summarize, we demonstrate that laser deposition frequency serves as an effective parameter for tuning the structural, optical, and magnetic properties of TiN–NiO VANs. XRD and STEM analysis confirm the formation of highly ordered pillar-in-matrix nanostructures, with pillar diameter and density strongly dependent on deposition frequency. Higher frequencies result in finer, more densely packed NiO pillars. In addition, ellipsometry measurements reveal that all samples exhibit a strong and tunable Type-II HMM behavior *i.e.*, positive permittivity perpendicular and negative permittivity in-plane. This confirms that dielectric permittivity can be engineered through growth kinetics, potentially enabling hyperbolic behavior with low optical loss over a wide spectral range.

Magnetic characterization further shows that the VAN nanostructures induce ferromagnetic-like behavior in NiO at both 10 K and 300 K, despite bulk NiO being antiferromagnetic. The correlation between these properties suggests strain-induced coupling and enhanced plasmon field localization at the interface between pillar and matrix, contributing to the emergent optical and magnetic behavior. These results establish a clear correlation between morphological control and tunable opto-magnetic functionalities through changing growth parameters. The ability to tune both hyperbolic optical properties and nanoscale magnetism through a single deposition parameter opens opportunities in novel metamaterial designs for magnetic sensors, optical modulators, and spintronic devices.

4 Experimental section

Thin film growth

The TiN–NiO thin films were grown on single-crystal MgO(001) substrates using Neocera pulsed laser deposition (PLD) chamber with a KrF excimer laser (Lambda Physik Compex Pro 205 λ = 248 nm). The TiN–NiO targets consists of a pie shaped NiO pasted on a TiN target, with a NiO volume ratio of 30%. The NiO pie shaped target was prepared by a conventional sintering and annealing process. The substrates were heated and maintained at 650 °C during deposition under high vacuum conditions (2.0×10^{-6} mbar). High vacuum conditions were kept during deposition and cooling process to suppress unwanted interdiffusion and chemical interaction. Laser frequency was controlled at 2, 5, and 10 Hz while keeping all other parameters constant. A pure TiN thin film was deposited under identical conditions and was used as a baseline reference.

Structural, optical, and magnetic characterization

X-ray diffraction (XRD) patterns were collected in θ–2θ geometry using a PANalytical X'Pert diffractometer with a Cu Kα_1 radiation source (λ = 0.15406 nm). Transmission electron microscopy (TEM) and scanning transmission electron microscopy (STEM) in high-angle annular dark-field (HAADF) mode were performed on a Thermo Fisher Scientific Talos F200X microscope with 1.6 Å point-to-point resolution. Cross-sectional and plan-view TEM specimens were prepared *via* standard methods involving mechanical grinding, polishing, and dimpling, followed by final ion milling using a Gatan PIPS 695 system. Spectroscopic ellipsometry was performed using a J.A. Woollam RC2 system at variable incidence angles (55°, 65°, and 75°) over the spectral range of 210–2500 nm. The real (ε_1) and imaginary (ε_2) components of the dielectric function were extracted by fitting the ellipsometry parameters Ψ and Δ using the Gen-Oscillator model in CompleteEASE software. Magnetic hysteresis measurements were completed with an MPMS Model 3 (Quantum Design) with EverCool SQUID magnetometer in the user facility of the Birck Nanotechnology Center at Purdue University see birck.research.purdue.edu. The magnetic moment *versus* applied field measurement was completed at both 300 K and 10 K up to a field of ±20 kOe in both the in-plane and out-of-plane direction.

Conflicts of interest

There are no conflicts to declare.

Data availability

The data that supports the findings of this study are available within the article and its supplementary information (SI). Supplementary information is available. The supplementary information includes additional XRD analysis results, indexed selected area diffraction pattern, cross-sectional TEM images, plan-view pillar density analysis, EDS mapping and line profiles, lattice parameter analysis using HRSTEM images, optical and magnetic property data for the samples deposited under various frequencies. See DOI: https://doi.org/10.1039/d6nr00994h.

Acknowledgements

This work was supported by the U.S. National Science Foundation DMR-2016453. The microscopy work was partially supported by Laboratory Directed Research and Development program at Sandia National Laboratories. Sandia National Laboratories is a multi-mission laboratory managed and operated by National Technology and Engineering Solutions of Sandia, LLC, a wholly owned subsidiary of Honeywell International, Inc., for the U.S. Department of Energy's National Nuclear Security Administration under contract no. DE-NA0003525. This work was performed, in part, at the Center for Integrated Nanotechnologies, an Office of Science User Facility operated for the U.S. Department of Energy (DOE) Office of Science by Los Alamos National Laboratory and Sandia National Laboratories. This paper describes objective technical results and analysis. Any subjective views or opinions that might be expressed in the paper do not necessarily represent the views of the U.S. Department of Energy or the United States Government.

References

1 P. Huo, S. Zhang, Y. Liang, Y. Lu and T. Xu, *Adv. Opt. Mater.*, 2019, 7(14), 1801616.
2 J. Lu, D. Zhang, R. L. Paldi, Z. He, P. Lu, J. Deitz, A. Ahmad, H. Dou, X. Wang, J. Liu, Z. Hu, B. Yang, X. Zhang, A. A. El-Azab and H. Wang, *Mater. Horiz.*, 2023, **10**, 3101–3113.
3 J. Liu, J. M. Lui, W. Sriturravanich, Y. Pikus, C. Sun and X. Zhang, *Nano Lett.*, 2005, 1726–1729.
4 K. E. Fong and L. Y. Yung, *Nanoscale*, 2013, **5**, 12043–12071.
5 A. V. Kimel and M. Li, *Nat. Rev. Mater.*, 2019, **4**, 189–200.

6 R. Esteban-Puyuelo, R. K. Sonkar, B. Pujari, O. Granas and B. Sanyal, *Phys. Chem. Chem. Phys.*, 2020, **22**, 8212–8218.
7 Z. Zhou, Z. Zheng, J. He, J. Wang, O. V. Prezhdo and T. Frauenheim, *Nano Lett.*, 2023, **23**, 5688–5695.
8 M. Dabrowski, J. N. Scott, W. R. Hendren, C. M. Forbes, A. Frisk, D. M. Burn, D. G. Newman, C. R. J. Sait, P. S. Keatley, A. T. N'Diaye, T. Hesjedal, G. van der Laan, R. M. Bowman and R. J. Hicken, *Nano Lett.*, 2021, **21**, 9210–9216.
9 K. T. Chang, W. Liang, Y. Lu and H. Lu, *npj Spintron.*, 2025, **3**, 44.
10 P. Gomez-Romero, A. Pokhriyal, D. Rueda-Garcia, L. N. Bengoa and R. M. Gonzalez-Gil, *Chem. Mater.*, 2024, **36**, 8–27.
11 J. Yao, Z. Liu, Y. Liu, Y. Wang, C. Sun, G. Bartal, A. M. Stacy and X. Zhang, *Science*, 2008, **321**, 930.
12 C. Enkrich, F. Pérez-Willard, D. Gerthsen, J. F. Zhou, T. Koschny, C. M. Soukoulis, M. Wegener and S. Linden, *Adv. Mater.*, 2005, **17**, 2547–2549.
13 A. Boltasseva and V. M. Shalaev, *Metamaterials*, 2008, **2**, 1–17.
14 J. Liu, X. Wang, X. Gao, H. Wang, J. Jian, J. Huang, X. Sun, Z. Qi, S. Misra, Z. He and H. Wang, *Appl. Mater. Today*, 2020, **21**(C), 100856.
15 D. Zhang, S. Misra, L. Li, X. Wang, J. Jian, P. Lu, X. Gao, X. Sun, Z. Qi, M. Kalaswad, X. Zhang and H. Wang, *Adv. Opt. Mater.*, 2019, **8**, 1901359.
16 N. A. Bhatt, R. L. Paldi, J. P. Barnard, J. Lu, Z. He, B. Yang, C. Shen, J. Song, R. Sarma, A. Siddiqui and H. Wang, *Crystals*, 2024, **14**(1), 65.
17 S. Misra and H. Wang, *Mater. Horiz.*, 2021, **8**, 869–884.
18 X. Wang and H. Wang, *Nanoscale*, 2020, **12**, 20564–20579.
19 X. Wang and H. Wang, *Chemosensors*, 2021, **9**(6), 145.
20 A. Chen and Q. Jia, *MRS Bull.*, 2021, **46**, 115–122.
21 A. Chen, Q. Su, H. Han, E. Enriquez and Q. Jia, *Adv. Mater.*, 2019, **31**, e1803241.
22 J. Huang, T. Jin, S. Misra, H. Wang, Z. Qi, Y. Dai, X. Sun, L. Li, J. Okkema, H. T. Chen, P. T. Lin, X. Zhang and H. Wang, *Adv. Opt. Mater.*, 2018, **6**(19), 1800510.
23 L. Quigley, J. Shen, J. Lu, C. A. Mihalko, J. P. Barnard, Y. Zhang, N. A. Bhatt, K. Evancho, R. Sarma, A. Siddiqui and H. Wang, *Cryst. Growth Des.*, 2024, **24**, 8929–8936.
24 J. Song and H. Wang, *J. Phys. Mater.*, 2025, **8**(1), 012002.
25 D. Zhang, P. Lu, S. Misra, A. Wissel, Z. He, Z. Qi, X. Gao, X. Sun, J. Liu, J. Lu, X. Zhang and H. Wang, *Adv. Opt. Mater.*, 2021, **9**(1), 2001154.
26 G. Palermo, K. V. Sreekanth, N. Maccaferri, G. E. Lio, G. Nicoletta, F. De Angelis, M. Hinczewski and G. Strangi, *Nanophotonics*, 2020, **10**, 295–314.
27 Y. Zhang, J. Shen, B. K. Tsai, X. Sheng, Z. Hu, X. Zhang and H. Wang, *Small Methods*, 2024, **8**, e2400087.
28 X. Gao, D. Zhang, X. Wang, J. Jian, Z. He, H. Dou and H. Wang, *Nanoscale Adv.*, 2020, **2**, 3276–3283.
29 G. V. Naik, A. Boltasseva and J. Kim, *Opt. Mater. Express*, 2011, **1**(6), 1090–1099.
30 B. Janaszek, A. Tyszka-Zawadzka and P. Szczepański, *IEEE J. Sel. Top. Quantum Electron.*, 2023, **29**, 1–9.
31 J. Huang, X. Wang, N. L. Hogan, S. Wu, P. Lu, Z. Fan, Y. Dai, B. Zeng, R. Starko-Bowes, J. Jian, H. Wang, L. Li, R. P. Prasankumar, D. Yarotski, M. Sheldon, H. T. Chen, Z. Jacob, X. Zhang and H. Wang, *Adv. Sci.*, 2018, **5**(7), 1800416.
32 R. Mishra, C.-W. Chang, A. Dubey, Z.-Y. Chiao, T.-J. Yen, H. W. Howard Lee, Y.-J. Lu and S. Gwo, *J. Phys. Chem. C*, 2021, **125**(24), 13658–13665.
33 X. Wang, Z. Qi, J. Liu, H. Wang, X. Xu, X. Zhang and H. Wang, *ACS Appl. Mater. Interfaces*, 2021, **13**, 39730–39737.
34 R. Karsthof, M. Grundmann, A. M. Anton and F. Kremer, *Phys. Rev. B: Condens. Matter Mater. Phys.*, 2019, **99**(23), 235201.
35 R. H. Kodama, S. A. Makhlouf and A. E. Berkowitz, *Phys. Rev. Lett.*, 1997, **79**, 1393–1396.
36 X. Wang, H. Wang, J. Jian, B. X. Rutherford, X. Gao, X. Xu, X. Zhang and H. Wang, *Nano Lett.*, 2020, **20**, 6614–6622.
37 Q. Jin, Z. Wang, Q. Zhang, Y. Yu, S. Lin, S. Chen, M. Qi, H. Bai, A. Huon, Q. Li, L. Wang, X. Yin, C. S. Tang, A. T. S. Wee, F. Meng, J. Zhao, J.-o. Wang, H. Guo, C. Ge, C. Wang, W. Yan, T. Zhu, L. Gu, S. A. Chambers, S. Das, T. Charlton, M. R. Fitzsimmons, G.-Q. Liu, S. Wang, K.-j. Jin, H. Yang and E.-J. Guo, *Phys. Rev. Lett.*, 2022, **128**, 017202.
38 B. Zhang, M. Kalaswad, B. X. Rutherford, S. Misra, Z. He, H. Wang, Z. Qi, A. E. Wissel, X. Xu and H. Wang, *ACS Appl. Mater. Interfaces*, 2020, **12**, 51827–51836.
39 J. Huang, W. Li, H. Yang and J. L. MacManus-Driscoll, *MRS Bull.*, 2021, **46**, 159–167.
40 W. Zhang, A. Chen, Z. Bi, Q. Jia, J. L. MacManus-Driscoll and H. Wang, *Curr. Opin. Solid State Mater. Sci.*, 2014, **18**, 6–18.
41 R. L. Paldi, X. Sun, X. Wang, X. Zhang and H. Wang, *ACS Omega*, 2020, **5**, 2234–2241.
42 A. Chen, Z. Bi, C. F. Tsai, J. Lee, Q. Su, X. Zhang, Q. Jia, J. L. MacManus-Driscoll and H. Wang, *Adv. Funct. Mater.*, 2011, **21**, 2423–2429.
43 J. Huang, Z. Qi, L. Li, H. Wang, S. Xue, B. Zhang, X. Zhang and H. Wang, *Nanoscale*, 2018, **10**, 17182–17188.
44 G. Hikosaka, Y. Shinohara, R. Matsumura, M. Nishida and T. Inamura, *Shap. Mem. Superelasticity*, 2025, **11**, 579–592.
45 D. Lee, S. So, G. Hu, M. Kim, T. Badloe, H. Cho, J. Kim, H. Kim, C.-W. Qiu and J. Rho, *eLight*, 2022, **2**.
46 L. Ferrari, C. Wu, D. Lepage, X. Zhang and Z. Liu, *Prog. Quantum Electron.*, 2015, **40**, 1–40.
47 J. Song, Z. He, C. Shen, J. Zhu, Z. Qi, X. Sun, Y. Zhang, J. Liu, X. Zhang, X. Ruan, P. Bermel and H. Wang, *Adv. Mater. Interfaces*, 2024, **11**(5), 2300733.
48 C. Moya, J. Ara, A. Labarta and X. Batlle, *Magnetism*, 2024, **4**, 252–280.
49 V. Verma and M. Katiyar, *J. Phys. D: Appl. Phys.*, 2015, **48**(23), 235003.
50 J. Liu, Y. Zhang, H. Dou, B. K. Tsai, A. Choudhury and H. Wang, *Sensors*, 2024, **24**(15), 4863.
51 M. Kalaswad, D. Zhang, B. X. Rutherford, J. Lu, J. P. Barnard, Z. He, J. Liu, H. Wang, X. Xu and H. Wang, *Crystals*, 2022, **12**(6), 849.
52 J. Song, D. Zhang, P. Lu, Y. Zhang, H. Wang, H. Dou, X. Xu, J. Deitz, X. Zhang and H. Wang, *ACS Appl. Mater. Interfaces*, 2023, **15**, 37810–37817.

53 J. Huang, B. K. Tsai, A. Choudhury, J. Shen, C. A. Mihalko, S. Zhou, C. Liu and H. Wang, *Adv. Mater. Interfaces*, 2025, **12**, e00613.
54 B. K. Tsai, J. Huang, Y. C. Yu, M. H. Lee, B. T. Stegman, E. J. Flores, P. Z. Tong, K. Xu, S. Zhou, J. Shen, J. Song, Y. Zhang, L. Stanciu, W. Wu, X. Zhang and H. Wang, *Adv. Funct. Mater.*, 2025, **35**(13), 2418004.
55 J. Shen, B. K. Tsai, K. Xu, A. Shang, J. P. Barnard, Y. Zhang, R. Tripathi, Z. Chen, X. Zhang and H. Wang, *Nano Res.*, 2023, **16**, 10559–10566.